

ARTICLE TYPE

First Use of GPS Satellites for Beam Calibration of Radio Telescopes

S. Berger,^{1,2,3,4} A. Lasinski,^{3,4,5} E. Egan,^{3,4} D. Wulf,^{3,4} A. Chokshi,^{1,2} and J. Sievers^{3,4}¹School of Physics, University of Melbourne, Parkville, VIC 3010, Australia²ARC Centre of Excellence for All Sky Astrophysics in 3 Dimensions (ASTRO 3D). Australia³Department of Physics, McGill University, Montréal, QC, H3A 2T8, Canada⁴Trottier Space Institute, McGill University, Montreal, QC, Canada⁵Department of Astronomy and Astrophysics, University of Toronto, Toronto, ON M5S 3H4, Canada

Author for correspondence: Sabrina Berger, Email: berger@student.unimelb.edu.au.

Abstract

We present results from the first application of the Global Navigation Satellite System (GNSS; GPS is one example of a collection of satellites in GNSS) for radio beam calibration using a commercial GNSS receiver with the Deep Dish Development Array (D3A) at the Dominion Radio Astrophysical Observatory (DRAO). Several GNSS satellites pass through the main and side lobes of the beam each day, enabling efficient mapping of the 2D beam structure. Due to the high SNR and abundance of GNSS satellites, we find evidence that GNSS can probe several side lobes of the beam through repeatable measurements of the beam over several days. Over three days of measurements, we find a measured difference reaching a minimum of 0.56 db-Hz in the main lobe of the primary beam. These results show promise for the use of GNSS in beam mapping for the Canadian Hydrogen Observatory and Radio-transient Detector (CHORD) and other future “large-N” radio interferometers. They also motivate future development of the technique within radio astronomy.

Keywords: 21cm cosmology, beam calibration, Global Navigational Satellite System**1. Introduction**

Detection of 21cm emission beyond the local universe requires an extremely accurate understanding of both telescope systematics and astrophysical foregrounds. Precise beam calibration and complementary foreground removal present some of the most critical challenges in future precision 21cm line intensity mapping experiments. The Canadian Hydrogen Observatory and Radio transient Detector (CHORD) is a new radio telescope with 21cm line intensity mapping amongst its primary science goals. CHORD will be constructed at the Dominion Radio Astrophysical Observatory (DRAO) near Penticton in British Columbia (Vanderlinde et al. 2019). Although each dish will be adjustable in declination, CHORD will operate primarily as a drift-scan instrument and will contain 512 dishes. It will build on the success of the Canadian Hydrogen Intensity Mapping Experiment (CHIME) by extending sensitivity to local universe 21cm emission and localizing fast radio bursts (FRBs) to milli-arcsecond precision while implementing several instrumental innovations. CHIME (also a drift-scan telescope) has recently cited beam calibration as one of its ongoing challenges in detecting Baryon Acoustic Oscillations (BAO) at low redshift (CHIME Collaboration 2022b).

CHORD has a frequency range of 300–1500 MHz spanning three times the frequency range of CHIME (400–800 MHz). A new technique using the Global Navigation Satellite System (GNSS) is a viable addition to beam calibration for CHORD. Notably, the frequency range of CHORD spans nearly the full range of GNSS frequencies. The Deep Dish Development Array (D3A) is a CHORD prototype experiment which consists of three six-meter dishes that function as an interferometer with a frequency range between 300

and 1600 MHz. The D3A is being built to refine CHORD’s new technologies. The key calibration scheme for CHORD requires consistent repeated measurements of the same interferometric modes, i.e., redundant calibration (Sievers 2017). Precise knowledge of the differences between the beam of each interferometric element is needed by ensuring both precise metrological and beam measurements. The dish has a surface precision design goal of one thousandth of a wavelength at 300 MHz (1mm). Advances in dish metrology (Islam and Ölçek 2020) have shown that current composite manufacturing processes can produce dishes that meet or exceed this requirement. This leaves the bottleneck for accurate redundant calibration to precision beam mapping.

Traditional beam mapping techniques use well known and radio bright astrophysical sources which drift-scan over the beam. This produces a measurement of the beam convolved with the radio source. Additionally, holographic methods have been explored to increase precision of beam mapping with astrophysical sources with the CHIME pathfinder. Berger et al. (2016) and CHIME Collaboration (2024) used measurements with the DRAO John A. Galt telescope which lies adjacent to the CHIME and future CHORD site. This allowed for measurements of the East to West beam structure to be made, but they only sparsely sample the beam in declination resulting in gaps in the North–South direction. Long integration times were also required for low signal-to-noise ratio (SNR) sources. CHIME has also relied on drift-scan only measurements of the beam with the Sun (CHIME Collaboration 2022a), but this relies heavily on solar variability being at a minimum. In the case of radio bright astrophysical sources, few are sufficiently bright to map the beams of individual sources into

the side lobes, and their fixed trajectories span a small solid angle. The design of "large-N", "small-D" interferometers allows for a large primary field of view (due to the small diameter and large number of elements). Because the primary field of view is designed to be much larger, beam mapping techniques with large solid angle coverage are especially useful. In recent years, beam calibration methods have extended from using celestial radio sources (Baars 1973), to employing artificial calibration sources such as drones (e.g., Chang et al. (2015); Bolli et al. (2016); Herman et al. (2024)). Using drones allows for precision control of the calibration. A drone can emit frequency dependent emission and tailor its flight path to the instrument covering the entirety of the beam. In Tyndall et al. (2024), the first drone-based beam measurement of a cylindrical radio interferometer was made with CHIME. The holographic (latest measurements in CHIME Collaboration (2024)), solar, and drone beams were similar, especially in indicating the location of the primary beam and side lobes. Measuring the far field beam pattern is challenging with most drones, especially at higher frequencies or with larger dishes (far field > than 300m for a D3A dish observing the 21cm line). In addition to drones, satellites present another prime artificial calibration source and except in the case of many Very Long Baseline Interferometry (VLBI) experiments always lie in the far field. For example, Orbcomm satellites were used to map the Murchison Widefield Array which operates at extremely lower frequencies around 100 MHz (Line et al. 2018; Chokshi et al. 2021).

There is also promise in using GNSS as a phase calibrator in VLBI to measure total electron content of the ionosphere at different sites, especially for localization of FRBs in real time. This is limited by the precision in comparing GNSS arrival times to those expected based on the satellite distance. FRBs are transients that go off at highly uncertain times, and there is usually not a readily available classic VLBI calibrator to use at the time of the burst. However, characterization of a GNSS receiver to the precision such that the use of GNSS for phase calibration could be useful requires an extremely thorough understanding of the receiver itself (Coster et al. 2013). Leading ionospheric mapping efforts are pushing down to a precision that is useful in VLBI fringe fitting, i.e., a relative total electron content (TEC) measurement at the 0.01 TECu level. However, utilizing the carrier phase to obtain extremely precise phase measurements may be possible because the GNSS measurements will be made on the same precision clocks as the VLBI instrument. The National Institute of Standards and Technology (NIST) has shown that frequency comparisons with a precision of 10^{-15} have been made over 24 hours of averaging (Larson and Levine 1998). This is ongoing research by NIST and Common View GPS Time Transfer. GNSS shows some promise for use as a prior in initial VLBI phase calibration.

Because there does not exist one perfect beam mapping technique for drift-scan instruments, multiple complementary techniques are often needed. GNSS satellites are a potential addition to the currently available beam mapping techniques. They overlap with low-z 21cm measurements with frequencies

spanning between approximately 1100-1600 MHz. They also lie in the far field of the D3A with orbits at an altitude of approximately 20,000 km. GNSS is an umbrella term for the many satellite constellations used in localization, timing, and atmospheric observations and contains greater than 100 high SNR far field satellites worldwide. The abundance of GNSS satellites could lead to more complete coverage of the CHORD beam at GNSS frequencies.

We present an overview of the first beam map measured using GNSS. We use an off-the-shelf commercially available GNSS receiver to provide an initial characterization of the D3A beam. In Section 2, we discuss the experimental setup, provide a brief overview of the GNSS mapping technique, and the commercial GNSS receiver. The first repeatable measurements of a radio telescope beam with GNSS are presented in Section 3. We conclude in Section 4 with a brief discussion of the potential for a radiometric measurement of the beam with GNSS in the future and the preliminary promise of GNSS beam calibration.

2. Experimental Setup

We provide a brief overview of the radio telescope beam, the D3A instrument, GNSS, and the commercial receiver (Septentrio Mosaic X-5 Receiver). We direct the reader to Wilson, Rohlf, and Hüttemeister (2009) and Misra and Enge (2011) for more extensive overviews of the radio telescope beam and GNSS, respectively.

2.1 Physical Radio Telescope Beams

Every radio telescope beam describes the sensitivity to different parts of the sky as a function of the angle of incoming radiation. Unless otherwise stated, "beam" will refer to the power pattern, which is equal to the square of the electric field strength. The beam's shape is determined by the aperture's shape and size and is very sensitive to subtle physical aberrations in the aperture. Every beam pattern follows the shape of the Fourier transform of the aperture, but this is not trivial with imperfect or non-uniform apertures. Within radio astronomy terminology, there also exists the synthesized beam which describes beams formed using multiple elements of a radio interferometer. We aim to map the physical radio telescope beam, referred to as the *primary beam* in this paper, or $P(\theta, \phi, \lambda)$, where θ is the altitude, ϕ is the azimuth, and λ is the observing frequency as described in Wilson, Rohlf, and Hüttemeister (2009). We can define the *normalized primary beam* as

$$P(\theta, \phi, \lambda)_n = \frac{1}{P_{\text{maximum}}} P(\theta, \phi, \lambda). \quad (1)$$

Most of the power within the radio telescope is collected within the *main lobe* which is the solid angle within the first null of the *primary beam*. The rest of the sphere of the beam are called the *side lobes* or back lobes. The angle that the main lobe subtends is called the *main beam solid angle* and is defined by

$$\Omega_{\text{main beam}} = \int_0^{2\pi} \int_0^{\pi} P(\theta, \phi, \lambda)_n \sin(\theta) d\theta d\phi. \quad (2)$$

We can also calculate the idealized beam pattern of the top-hat circular aperture as a slice of the Airy pattern. The intensity of the Airy pattern is the square of the Fourier transform of the aperture

$$I(\theta) = I_0 \left[\frac{2J_1(kr \sin(\theta))}{kr \sin(\theta)} \right]^2, \quad (3)$$

where I_0 is the maximum intensity of the beam, J_1 is a first order Bessel function of the first kind, $k = \frac{2\pi}{\lambda}$ or the wavenumber of the observing frequency, r is the radius of the aperture (3m for the D3A), and θ is the angle from the axis of the circular aperture. Note that the azimuthal component (ϕ) does not matter as the idealized Airy beam is spherically symmetric.

In the idealized case for a dish with a circular aperture, the full width half maximum (FWHM), or when $P(\theta, \phi, \lambda) = 0.5$, is equivalent to that of an Airy disk and the expression can be derived from Equation 3 as

$$\theta_{\text{FWHM}} = 1.029 \frac{\lambda}{d}, \quad (4)$$

where λ is the observing frequency and d is the diameter of the dish. This is sometimes referred to as the equivalent width of the main lobe. Modeling the expected power beam often requires taking the full signal chain into account. We do not compare our observations with GNSS to those calculated using a simulated D3A dish in an EM field solver such as CST Studio Suite, but it's beam still resembles the Airy disk to first order.

2.2 The Deep Dish Development Array (D3A)

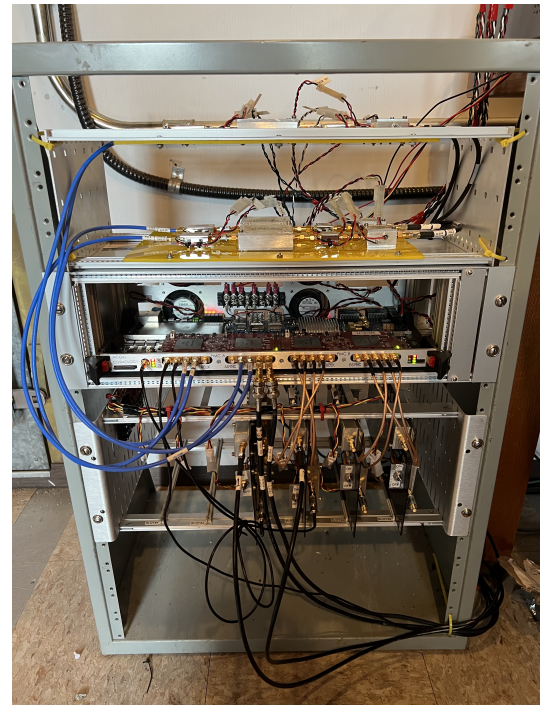
CHORD is the next generation large scale radio telescope in Canada. It will be located adjacent to CHIME at the DRAO. Following after the large success of CHIME in both cosmology and FRBs, CHORD will tailor its science goals with lessons learned from CHIME, including the detection of 1000s of FRBs localized to milli-arcsecond precision, pulsar and galaxy science after Cosmic Noon, magnetic fields in the universe, and 21cm intensity mapping.

The D3A serves as an early prototype for CHORD and consists of 3 six-meter dishes. It is currently used to test a variety of new techniques that will be needed for CHORD, including metrology and ultra-wideband receivers. One of the six-meter dishes can be seen in the top panel of Figure 1. Each dish has an ultra-optimized focal ratio ($f/D = 0.25$ for D3A, currently but $f/D = 0.21$ for CHORD) and a modified Vivaldi feed as described in Mackay et al. (2023). D3A observes at frequencies between 300–1600 MHz, covering everything but the highest GNSS frequencies. The full electronics rack with the various RF chains is shown at the bottom of Figure 1. After amplification and filtering, the RF signal is split into three different bands with a prototype triplexer: roughly 400–800 MHz, 800–1200 MHz, and 1200–1600 MHz. The FWHM of the beam at center of the three bands in the triplexer, $\theta_{\text{FWHM,airy}} = 4.9^\circ, 2.9^\circ, 2.1^\circ$, respectively. Typically, the analog to digital conversion is done employing multiple ICE boards (Bandura et al. 2016) which digitizes the

signal to a precision of 8-bit. However in creating GNSS beam maps using a commercial receiver, we take the RF signal prior to processing with the ICE boards. Radiometric beam measurements made with GNSS in the future will require pre-processing data at the voltage level from the ICE boards. The power level of the D3A is set for this scale and has an absolute power of -20 dBm over 400 MHz of bandwidth. We found that attenuating this output by 3 dB produced a signal level that was well-matched to the input of the Septentrio Receiver.



(a) A D3A prototype dish



(b) D3A's RF backend

Figure 1. Top: One of the three 6m D3A dishes currently at the DRAO. CHORD will include 512 similar dishes situated next to the main CHIME site. Bottom: The backend of the D3A. The bottom crate slot contains the triplexer used in data collection. The middle part of the crate shows the ICE boards normally used in processing the D3A signal.

2.3 GNSS

GNSS is an umbrella term for the many constellations of satellites used in localization and atmospheric observations, including the Global Positioning Systems (GPS). They emit at a wide range of frequencies between 1100–1605 MHz. GNSS can provide measurements of power and phase at up to 40 or more locations in the sky at all times. There are times when more than one GNSS satellite is within the primary beam or sidelobes, but since the precise position of the satellite is always known with time, detangling the satellite signals is possible. The large variability in transit angle and high number of satellites makes the use of GNSS in beam calibration advantageous.

The various GNSS systems include GPS (United States), Global Navigation Satellite System (GLONASS from Russia), Galileo (European Union), and BeiDou (China). The true transmit power of GNSS satellites is not available to the public (Donaldson et al. 2020). However, we expect the power to remain relatively constant as compared to other satellite constellations such as Orbcomm. GNSS satellites do not release their broadcast power, though their directivity, defined as the ratio of intensity in one direction to the average intensity in all directions, is reasonably well known for some satellites. The directivity and gain patterns for GPS satellites are available (Marquis and Reigh 2015), and we plot the directivity of GPS Space Vehicle Number (SVN) 61 (also known as GPS IIR-13 and USA-180) in Figure 2. These data values are from the improved antenna panel onboard SVN 61 which increases the power near the edge of the Earth. The directivity measurements were measured with an uncertainty of ± 0.25 dB by Lockheed Martin. As shown in 2, the primary beams of GNSS satellites are engineered to be azimuthally symmetric and nearly constant across the full face of the Earth. For this reason, in this work we assume the received power to be constant over each satellite track. Each GNSS satellite has a unique, nearly temporally invariant beam profile that could be measured with an adjacent omnidirectional GNSS antenna. If the antenna is characterized in an anechoic chamber, as is commonly done in radio astronomy, the precise power of the GNSS emission beam can be measured. Although we do not use a supplementary antenna in this work, it will be essential in making absolute power measurements for future GNSS beam mapping.

In GNSS, the most common measurement of power is C/N_0 or carrier to noise power density ratio in dB-Hz. It is the ratio between the received power and the noise. Since we do not have a reference antenna to compare our measurements to, we do not convert to an absolute measurement when determining the average and standard deviation as described in Section 3.2. As seen in Donaldson et al. 2020, the usage of a reference antenna to determine an absolute power measurement by combining measurements using a best fit least-squares approach is a common approach. A similar method could be applied with antennas adjacent to future CHORD dishes and will be required for the precision beam measurements needed for 21cm observations.

We express the GNSS power as a carrier to noise measurement: C/N_0 [dB-Hz]. This is the most common way GNSS receivers report power. It expresses the carrier power to noise ratio per unit bandwidth. Typical values for L1 C/A C/N_0 are in the range between 37–45 dB-Hz, but we see higher values due to the large aperture of the D3A. C/N_0 can also be expressed in terms of a signal to noise ratio with

$$SNR = C/N_0 - BW, \quad (5)$$

where for L1 the spectrum spread (BW) is approximately 2 MHz. We can use this bandwidth to convert from C/N_0 values to an approximate value of SNR.

GNSS satellites orbit in medium Earth orbit (MEO) at approximately 20,000 km above the Earth's surface. They do not have consistent orbits which pass over the same part of Earth everyday at the same time. GPS uses six orbital planes with four satellites per plan. Although we do not account for it here, nodal precession, the change in the satellite's orbital plane due to gravitational perturbations predominantly from the Earth, must be accounted for in future beam maps made with GNSS. The nodal regression rate of the satellites is approximately -0.04 degrees/day (United States. Department of Defense 2020). Although we do not account for errors in orbital configuration from nodal regression or the launch of the satellite in this preliminary study, this effect should be accounted for in future beam maps made with GNSS.

The GNSS signal structure (Süzer and Oktal 2017; Raghavan, Shane, and Yowell 2006) is complex and varies based on the type of satellite. Because of this, we focus primarily on describing GPS and the general GNSS signal characteristics. Each GPS center frequency is a multiple of the 10.23 MHz master GPS clock. GPS frequencies are all in the L-band and are named as follows: L5 = 1176.45MHz = 115×10.23 MHz, L2 = 1227.6MHz = 120×10.23 MHz, L1 = 1575.42MHz = 154×10.23 MHz. Several satellites can transmit at the same frequency due to code division multiple access (CDMA). For GPS, this is accomplished with pseudorandom noise (PRN) codes. Each satellite has a particular PRN code corresponding to its space vehicle number which allows the GNSS receiver to disentangle visible satellites from a frequency. The GNSS satellite modulates a carrier wave with a binary PRN code with various modulation schemes. In the United States, there are currently approximately 31 GPS satellites in orbit to localize positions and thus 31 unique PRN codes. Each of the other GNSS satellites in the international array also has an associated unique PRN code. This number changes each year as new satellites are launched and decommissioned. For GPS, there is both the Course Acquisition (C/A) and military precision (P-code) with chipping rates of 1.023 Megachips/s and 10.23 Megachips/s, respectively. C/A codes repeat every millisecond after 1023 chips whereas P-codes repeat weekly. Commercial receivers can decode only C/A codes because P-codes are still encrypted by the US government.

For the L1 GPS signal, the PRN is modulated into a GPS carrier wave through the binary phase shift key (BPSK) modulation scheme. The binary message is encoded in the PRN

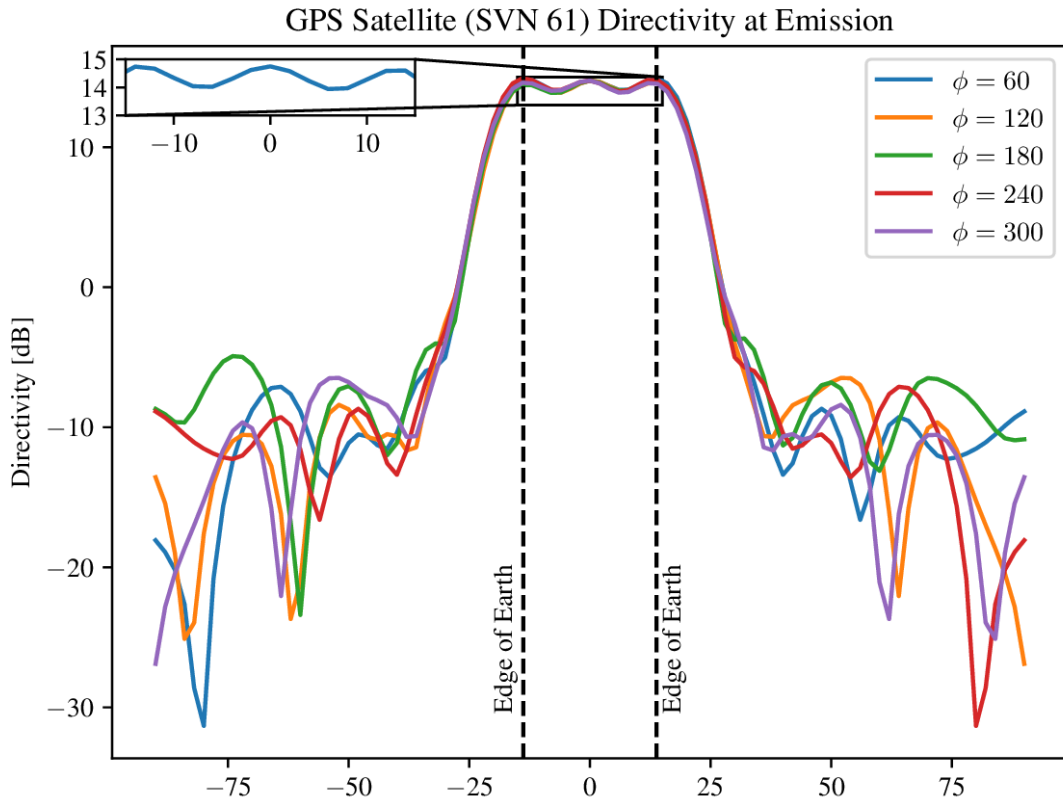


Figure 2. Plot of GPS SVN 61’s directivity at emission, i.e., characterized from the on-satellite antenna panel. The zoomed in plot exemplifies the fact that there’s only up to about 2 dB power loss across the Earth. The data used to make this plot were taken in 10 degree increments from the US Coast Guard Navigation Website.

code using two different phases of the carrier wave. $\theta = 0^\circ$ corresponds to a binary value of 1 and $\theta = 180^\circ$ corresponds to a binary value of 0. However, this modulation scheme is not standardized across all of GNSS or even GPS. For example, Beidou’s individual signals vary in modulation schemes from BPSK at 1176.45 MHz to Quadrature Multiplexed Binary Offset Carrier (QMBOC) at 1575.42 MHz. The GPS PRNs create GPS signals that are spread spectrum with a frequency range of about 20 MHz. Navigation data is modulated in at 50 bits per second and includes satellite ephemeris data and health status.

For the GPS L1 signal (Misra and Enge 2011), the signal can be described as follows where each variable shown in Equation 6 is described briefly in Table 1,

$$s(t) = \sqrt{2P_c}N(t)PRN(t) \cos(2\pi ft + \theta) + \sqrt{2P_p}N(t)P_{code}(t) \sin(2\pi ft + \theta). \quad (6)$$

2.4 The Septentrio Mosaic X-5 Receiver

The Septentrio Mosaic X-5 development kit and receiver is a commercially available GNSS receiver. The Septentrio Mosaic-

Table 1. Overview of variables shown in equation 6 which describes the signal as a function of time.

Variable	Brief Description
P_c	Amplitude of the C/A code
P_p	Amplitude of the P-code
$N(t)$	Navigation data
$PRN(t)$	C/A code as pseudorandom noise code
f	Frequency of signal (L1 here)
$P_{code}(t)$	Military P-code
$\sin(2\pi ft + \theta)$	RF carrier

X5 module is seen in Figure 3 on top of the development kit itself. There are an array of ways to connect to the receiver including micro-USB, ethernet, and serial ports. We collected data with a PC attached via micro-USB while the receiver is connected to the RF output of the D3A. We used a 3 dB attenuator between the output of the D3A signal and the Septentrio receiver to attenuate the RF output. There is also a bandpass filter that acts as a DC block for the 5V usually used to power the active GNSS antenna. The Mosaic X-5 has 448

hardware channels and supports simultaneous tracking of all publicly available and visible satellite signals. It is often updated to include new frequencies and satellites. GNSS receivers work by correlating all potential satellite template signals with the actual received signals at different time delays using matched filtering. This allows the receiver to detect, acquire, and track all visible GNSS satellites even in noisy environments.

Septentrio reports a horizontal and vertical accuracy of 0.6 cm and 1 cm, respectively, or approximately 30 picoseconds. This does not have an impact on beam mapping but could be important if GNSS is used as a phase/time calibrator. More relevantly, Septentrio lists a resolution for C/N_0 measurements of 0.03125 db-Hz. They also report less than 45 seconds to a satellite lock after turning the module on, which is consistent with our observations in this study. Septentrio also includes a suite of tools to analyze the GNSS data, namely RxTools, which we use to extract GNSS power, position and satellite names in our own beam mapping analysis. We use the GNSS measurements from the SBF (Septentrio Binary Format) files.

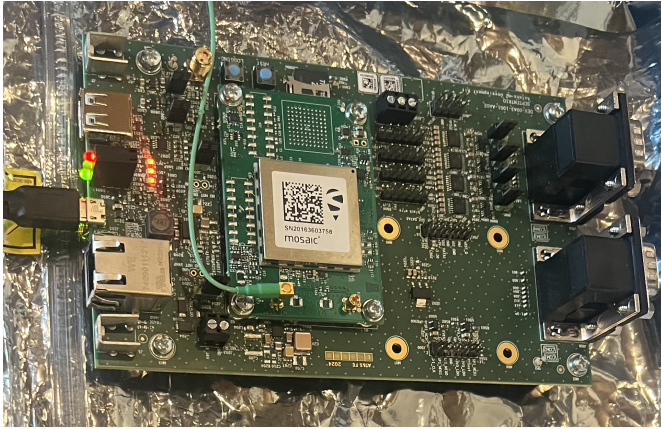


Figure 3. The Septentrio Mosaic X-5 receiver. The receiver can be connected to any computer through a micro-USB port as shown here. The LED lights near the micro-USB port indicate the receiver is on. To check whether the receiver and connected antenna are receiving any satellites, a web server can be opened on a browser on any Windows computer. The RF input comes through the green wire's micro-SMA port. The Mosaic X-5 GNSS module sits on top of the development kit and extracts information from visible GNSS antennas. The receiver was connected to the RF output from D3A.

3. GNSS D3A Beam Mapping Results

3.1 Satellite Tracks

We use data taken over approximately three days between August 30, 2022 at 00:21:57 UTC to September 2, 2022 at 19:25:37 UTC. The D3A dish was pointed at (altitude, azimuth) = (80.5°, 0°). We observe more than 80 satellites through one dish of the D3A in the 800-1200 MHz and 1200-1600 MHz output bands of the triplexer. We use the L1 frequency band (1575 MHz). This is due to seeing the most consistent and powerful measurements at L1 in these preliminary observations. There are 45 satellites which pass within 10 degrees of the center of the beam. The maximum binned power for tracks of the satellites seen over the course of approximately 72 hours through the D3A are shown in Figure

4. These include satellites from GPS, GLONASS, and Galileo. We zoom into altitudes close to the D3A beam center to clearly see the sharp increase in power as the satellites pass near boresight.

3.2 Individual Beam Slices

When we separate out slices of beam maps made by individual satellites, we see repeatable measurements made over multiple days. We plot each satellite's measured beam power as a function of angle from boresight, θ . We approximate θ by taking the dot product in Cartesian coordinates between the D3A location and satellite location. To allow for comparison over multiple days, we do not account for the azimuthal variations in the beam for each beam pass and limit our comparisons to the main lobe. This can be seen in Figures 5 (in time) and 6 (in angle from boresight). We plot the *raw* output beam data from the Septentrio receiver with minimal processing. The shape of the beam profiles varies as each cuts through a different slice of the beam. Each of the individual satellite beam profiles in Figure 5 shows the data over the days of acquisition. We offset the beam profile each day to show the repeatability in time. In Figure 6, we convert the beam profiles into an averaged angle from boresight. Since we did not have an external reference GNSS antenna, this means that the D3A beam pattern we plot also includes the GNSS transmission beam. However as seen in Figure 2, we expect less than a 3 dB difference across the Earth. We do not account for this in these preliminary measurements.

Each beam map shows repeatability in the primary lobes that worsens in the side lobes. The satellite does not pass through the exact same trajectory each day. We speculate that this is the cause of much of the variability in the side lobes. The D3A could be positioned to allow for a GNSS satellite to pass exactly through boresight, but in the sample satellites, we see gaps in the primary beam where the satellites pass close by but not exactly through boresight.

Despite high variance in some of the side lobes, which we hypothesize is largely due to azimuthal variations, we find reasonable agreement between the satellites shown. For the GPS satellites, G23 and G29, we find the smallest difference of 0.56 db-Hz in the primary lobe of the beam. The average power is averaged in log space due to not being able to convert to an absolute power measurement. Similarly, the standard deviation is calculated as follows in log space,

$$\sigma = \sqrt{\frac{\sum_N (C/N_0 - \bar{C/N_0})^2}{N}}, \quad (7)$$

where N is the number of passes the satellite makes through a particular altitude and azimuth. The average number of passes per measurement is 3. As seen in Table 2, the standard deviation is minimum at the peak of the beam measurement for satellite G04 at 0.09 db-Hz. This shows promising repeatability for future GNSS beam mapping experiments.

The mismatch in many of these satellite tracks may be partially due to the satellite nodal precession which occurs

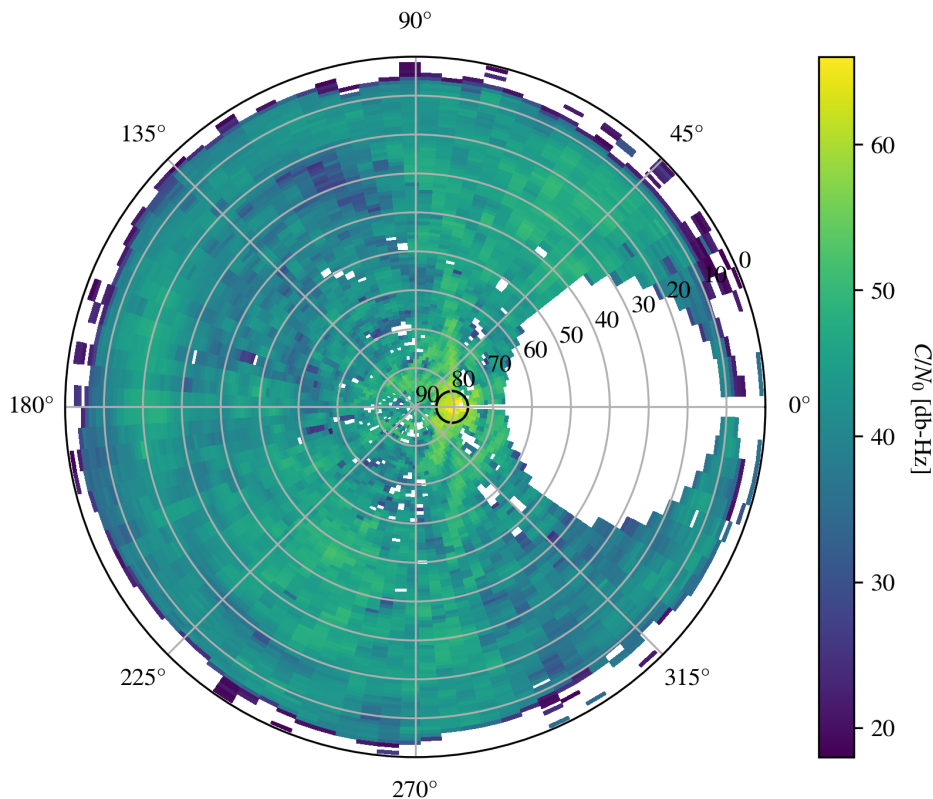


Figure 4. Satellites seen in L1 (For GPS, L1 is at 1575.42 MHz) tracks visible from the D3A at DRAO over approximately three days between August 30, 2022 at 00:21:57 UTC to September 2, 2022 at 19:25:37 UTC taken with the Septentrio Mosaic X-5 receiver. We bin the satellite tracks into 10,000 bins in altitude and azimuth in polar coordinates. These include satellites from GPS, GLONASS, and Galileo. The maximum binned power (C/N_0) at a particular position is plotted in color. The beam center is plotted in a black circle centered at (altitude, azimuth) = (80.5°, 0°). Note that the power plotted here is a raw output from the Septentrio receiver and includes both the GNSS beam transmission and D3A power.

daily at a rate of approximately half a degree. Each day the satellite does not pass through the exact same part of the beam as the day before also adding to the variance. This is described in more detail at the end of Section 2.3. However, we expect the majority of the errors to be due to the lack of a reference antenna.

4. Conclusions

Beam maps are a significant bottleneck to pushing precision measurements of the early universe. There have been many proposed methods for beam mapping beyond the classic astrophysical calibrator such as drones and satellites. Eventually, specific GNSS channels could be added to the CHORD correlator to make more precise beam measurements in lieu of an off the shelf receiver. This could provide an avenue for lossless recovery of measurements for low- z 21cm galaxies. At lower frequencies, beam measurements can be made with classic radio beam calibrators such as bright point sources and pulsars. Pulsar calibrators can also be used over the entire frequency band when they transit the beam. In FRB science, GNSS could aid in the measurement of more precise power measurements of FRBs detected in the sidelobes because of the preliminary success of measuring into the beam sidelobes at GNSS frequencies. However because 21cm intensity mapping

requires detections of a signal $10^5 - 10^6$ times dimmer than the noise, the 21cm intensity mapping will benefit the most from an extremely precise understanding of the beam.

We find that GNSS could be a powerful tool for mapping the beams of radio telescopes that observe at the L1 GNSS frequency range near 1600 MHz through repeatable beam measurements measured over several passes with multiple satellites. The measurements of far side lobes with GNSS is especially promising as this is a difficult problem in ongoing beam calibration using more traditional techniques. Although we have not considered full beam simulations accounting for the full RF pipeline in this work, we expect this to be an insightful next step in continuing exploration of this beam mapping method. Through the use of an external GNSS antenna and correcting for nodal precession and varying GNSS orbits, we can further improve our precision of beam maps created with this method. Plans to create an infrastructure to observe GNSS at baseband and utilize an external antenna remain open for future work.

Acknowledgement

S.B. thanks Vincent Mackay, Dillon Dong, and Jack Line for useful discussions about the presentation of the initial beam measurements. S.B. is also grateful Matt Dexter, Dan Werthimer, Alexander Abajian, and Quang Tran for helpful

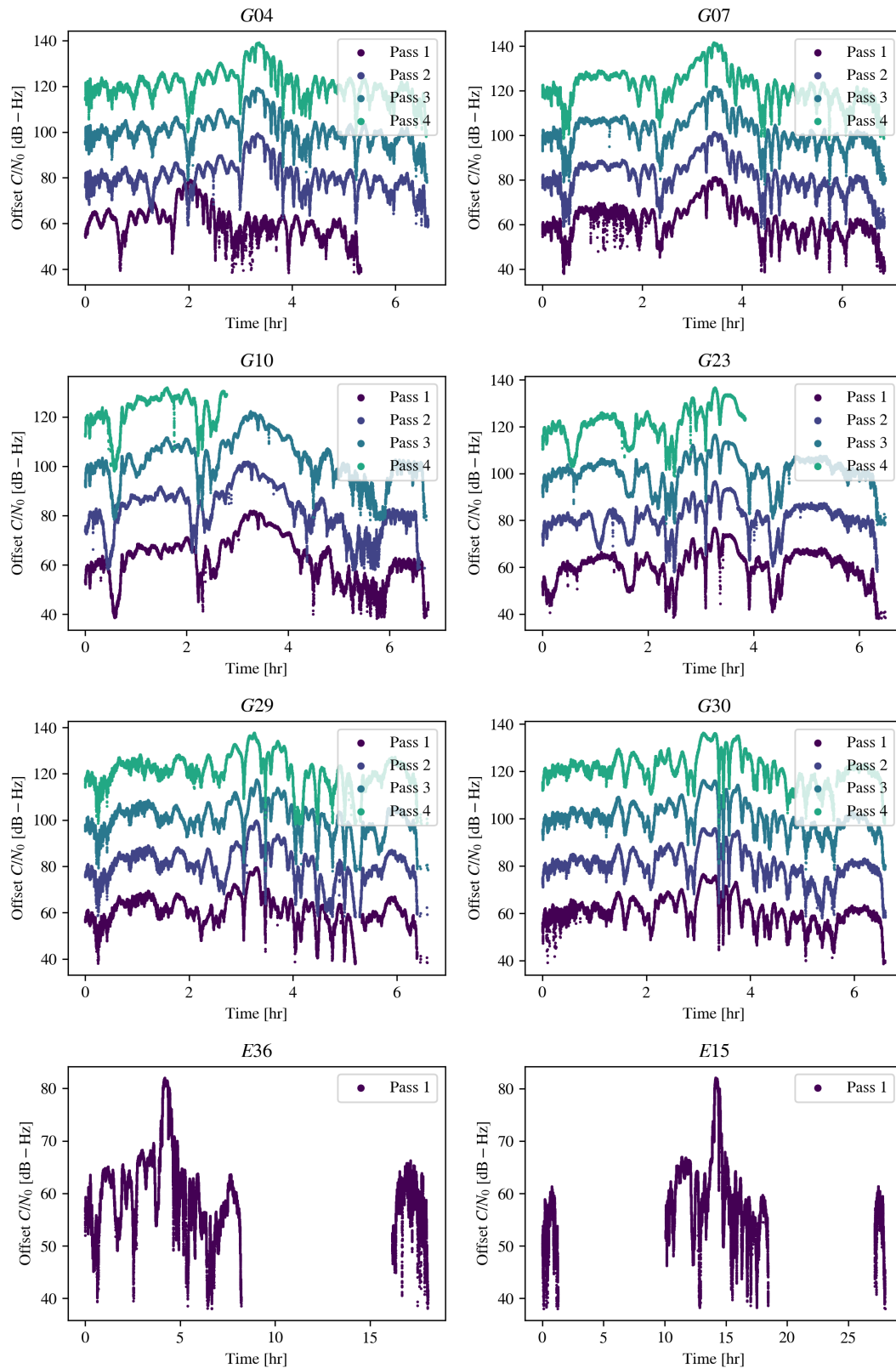


Figure 5. A selection of satellites denoted by their RINEX codes that pass within 5 degrees of the center of the beam. All observations are of the L1 frequency (1575 MHz). Each satellites' carrier to noise power (C/N_0) is plotted as a function of time since the start of a pass near the D3A. This data was taken over approximately three days between August 30, 2022 at 00:21:57 UTC to September 2, 2022 at 19:25:37 UTC. Each pass of the satellites' trajectory is plotted at 20 dB-Hz offset in power. We only include passes of the satellite that are more than 500 measurements long. Note that the power plotted here is a *raw* output from the Septentrio receiver and includes both the GNSS beam transmission and D3A power.

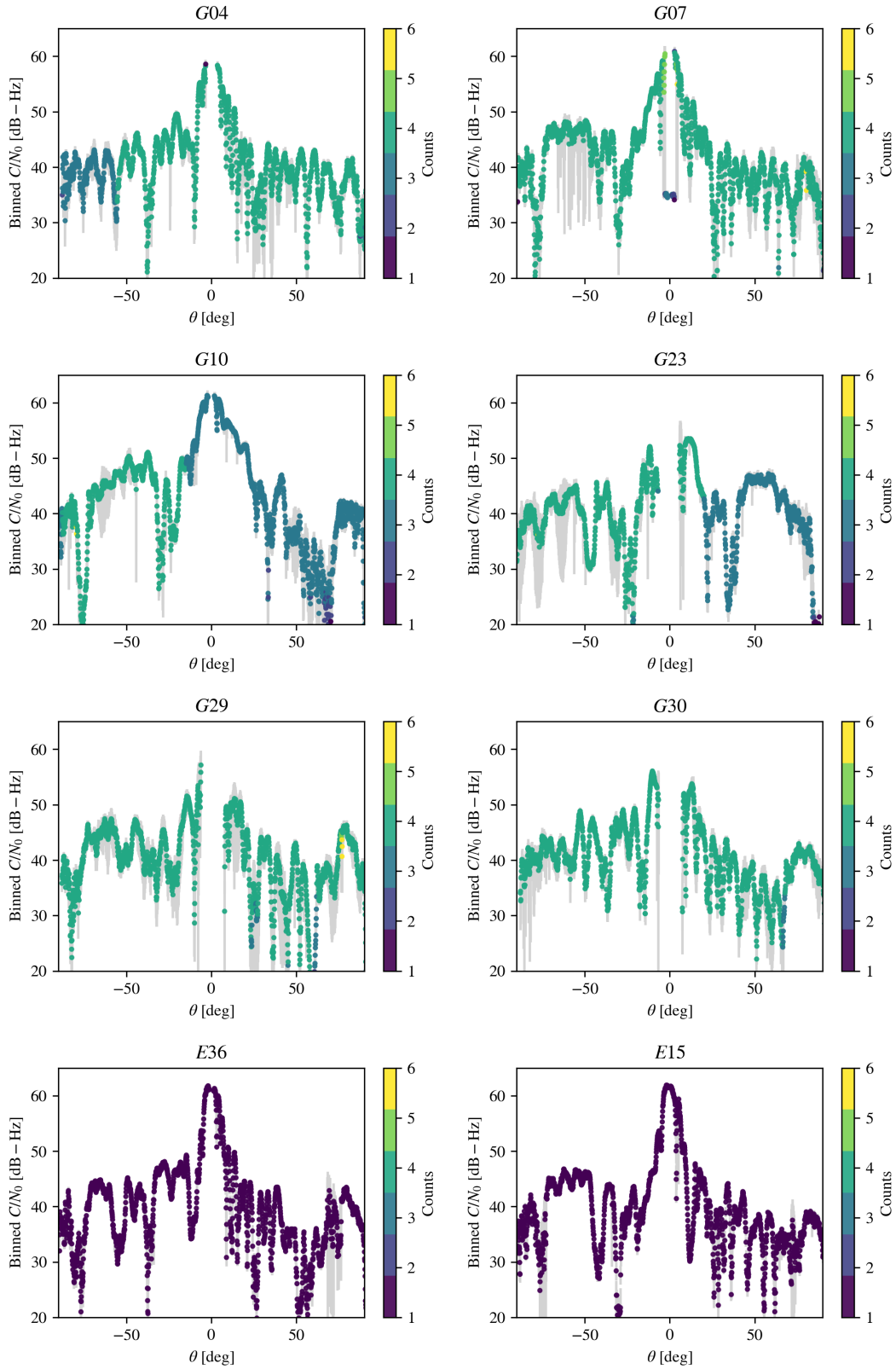


Figure 6. Same satellites as in Figure 5 with converted averaged C/N_0 and angle from boresight. The power measurement is averaged from the measurements shown in Figure 5 over August 30, 2022 at 00:21:57 UTC to September 2, 2022 at 19:25:37 UTC. Each satellites' carrier to noise power (C/N_0) is plotted as a function of angle from the center of the beam (θ). We note that azimuthal variations in passes are not taken into account, and many of the variations outside of the main lobe are due to this. We average the power measurements of each point into widths of 0.1 degree. Thus, the number of counts does not directly relate to the number of passes in Figure 5. The error bar is shown in light gray and shows the full range of power measurements made in the bin. The pattern clearly repeats each day as the satellite transits near the center of the beam at 0° . Note that the power plotted here is a *raw* output from the Septentrio receiver and includes both the GNSS beam transmission and D3A power.

Table 2. We tabulate the minimum C/N_0 difference at each measured angle (maximum - minimum C/N_0) across all angles for each satellite. We show the peak C/N_0 measurements for each GPS satellite alongside the corresponding σ value at that angle. Each σ value is calculated for angles at exactly the same degree as the observed value and described in Section 3. This exemplifies the small variance we see in measurements of the primary lobe of the beam. We also show the max σ per satellite which is the highest value seen throughout all angles measured from boresight. We do not include the GLONASS (E36 and E15) satellites in this Table due to lack of passes. .

Satellite	Max - Min C/N_0 [db-Hz]	Peak C/N_0 [db-Hz]	σ at Peak C/N_0 [db-Hz]	Max σ [db-Hz]
G04	1.69	57.25	0.09	4.97
G07	1.00	61.36	0.11	4.28
G10	0.94	56.68	0.16	6.19
G23	0.56	51.19	0.10	4.80
G29	0.56	59.48	0.11	8.46
G30	1.44	56.22	0.17	3.02

conversations and the use of lab space and equipment that aided in the completion of this paper. SB is supported by the Melbourne Research Scholarship and N D Goldsworthy Scholarship for Physics. This research made use of Python packages NumPy (Harris et al. 2020), Matplotlib (Hunter 2007), AstroPy (Astropy Collaboration et al. 2013; Astropy Collaboration et al. 2018; Astropy Collaboration et al. 2022), and SciPy (Virtanen et al. 2020). We acknowledge that the DRAO is located on the traditional, ancestral, and unceded territory of the Syilx/Okanagan people.

Competing Interests None

Data Availability Statement The code used in the data analysis can be found on GitHub here. RxTools, Septentrio's suite of data analysis and acquisition tools, can be found here.

References

- Astropy Collaboration, A. M. Price-Whelan, B. M. Sipőcz, H. M. Günther, P. L. Lim, S. M. Crawford, S. Conseil, et al. 2018. The Astropy Project: Building an Open-science Project and Status of the v2.0 Core Package. *The Astronomical Journal* 156, no. 3 (September): 123. <https://doi.org/10.3847/1538-3881/aabc4f>. arXiv: 1801.02634 [astro-ph. IM].
- Astropy Collaboration, Adrian M. Price-Whelan, Pey Lian Lim, Nicholas Earl, Nathaniel Starkman, Larry Bradley, David L. Shupe, et al. 2022. The Astropy Project: Sustaining and Growing a Community-oriented Open-source Project and the Latest Major Release (v5.0) of the Core Package. *ApJ* 935, no. 2 (August): 167. <https://doi.org/10.3847/1538-4357/ac7c74>. arXiv: 2206.14220 [astro-ph. IM].
- Astropy Collaboration, T. P. Robitaille, E. J. Tollerud, P. Greenfield, M. Droettboom, E. Bray, T. Aldcroft, et al. 2013. Astropy: A community Python package for astronomy. *Astronomy & Astrophysics* 558 (October): A33. <https://doi.org/10.1051/0004-6361/201322068>. arXiv: 1307.6212 [astro-ph. IM].
- Baars, J. 1973. The measurement of large antennas with cosmic radio sources. *IEEE Transactions on Antennas and Propagation* 21 (4): 461–474. <https://doi.org/10.1109/TAP.1973.1140521>.
- Bandura, K., A. N. Bender, J. F. Cliche, T. de Haan, M. A. Dobbs, A. J. Gilbert, S. Griffin, et al. 2016. *Ice: a scalable, low-cost fpga-based telescope signal processing and networking system*. <https://doi.org/10.48550/ARXIV.1608.06262>. <https://arxiv.org/abs/1608.06262>.
- Berger, Philippe, Laura B. Newburgh, Mandana Amiri, Kevin Bandura, Jean-François Cliche, Liam Connor, Meiling Deng, et al. 2016. Holographic beam mapping of the CHIME pathfinder array. In *SPIE proceedings*, edited by Helen J. Hall, Roberto Gilmozzi, and Heather K. Marshall. SPIE, August. <https://doi.org/10.1117/12.2233782>. <https://doi.org/10.1117/12.2233782>.
- Bolli, Pietro, F. Paonessa, Giuseppe Pupillo, G. Virone, M. J. Arts, Andrea LINGUA, Jader Monari, and Stefan Wijnholds. 2016. Antenna pattern characterization of the low-frequency receptor of lofar by means of an uav-mounted artificial test source, 99063V. July. <https://doi.org/10.1117/12.2232419>.
- Chang, Chihway, Christian Monstein, Alexandre Refregier, Adam Amara, Adrian Glauser, and Sarah Casura. 2015. Beam calibration of radio telescopes with drones. *Publications of the Astronomical Society of the Pacific* 127, no. 957 (November): 1131–1143. <https://doi.org/10.1086/683467>. <https://doi.org/10.1086/683467>.
- CHIME Collaboration. 2022a. *The Astrophysical Journal* 932, no. 2 (June): 100. <https://doi.org/10.3847/1538-4357/ac6b9f>. arXiv: 2201.11822 [astro-ph. IM].
- . 2022b. *Detection of cosmological 21 cm emission with the canadian hydrogen intensity mapping experiment*. <https://doi.org/10.48550/ARXIV.2202.01242>. <https://arxiv.org/abs/2202.01242>.
- . 2024. *Holographic beam measurements of the canadian hydrogen intensity mapping experiment*. arXiv: 2408.00172 [astro-ph. IM]. <https://arxiv.org/abs/2408.00172>.
- Chokshi, A, J L B Line, N Barry, D Ung, D Kenney, A McPhail, A Williams, and R L Webster. 2021. Dual polarization measurements of mwa beam-patterns at 137mhz. *Monthly Notices of the Royal Astronomical Society* 502, no. 2 (January): 1990–2004. issn: 1365-2966. <https://doi.org/10.1093/mnras/stab156>. <http://dx.doi.org/10.1093/mnras/stab156>.
- Coster, A., J. Williams, A. Weatherwax, W. Rideout, and D. Herne. 2013. Accuracy of gps total electron content: gps receiver bias temperature dependence. *Radio Science* 48 (2): 190–196. <https://doi.org/https://doi.org/10.1002/rds.20011>. eprint: <https://agupubs.onlinelibrary.wiley.com/doi/pdf/10.1002/rds.20011>. <https://agupubs.onlinelibrary.wiley.com/doi/abs/10.1002/rds.20011>.
- Donaldson, Jennifer E., Joel J.K. Parker, Michael C. Moreau, Dolan E. Highsmith, and Philip D. Martzen. 2020. Characterization of on-orbit gps transmit antenna patterns for space users. *NAVIGATION* 67 (2): 411–438. <https://doi.org/https://doi.org/10.1002/navi.361>. eprint: <https://onlinelibrary.wiley.com/doi/abs/10.1002/navi.361>.
- Harris, Charles R., K. Jarrod Millman, Stéfan J. van der Walt, Ralf Gommers, Pauli Virtanen, David Cournapeau, Eric Wieser, et al. 2020. Array programming with NumPy. *Nature* 585, no. 7825 (September): 357–362. <https://doi.org/10.1038/s41586-020-2649-2>. <https://doi.org/10.1038/s41586-020-2649-2>.

- Herman, Lawrence, Christopher Barbarie, Mohan Agrawal, Vlad Calinescu, Simon Chen, H. Cynthia Chiang, Cherie K. Day, et al. 2024. Drone-Based Antenna Beam Calibration in the High Arctic. *arXiv e-prints* (June): arXiv:2407.00856. <https://doi.org/10.48550/arXiv.2407.00856>. arXiv: 2407.00856 [astro-ph.IM].
- Hunter, J. D. 2007. Matplotlib: a 2d graphics environment. *CiSE* 9 (3): 90–95. <https://doi.org/10.1109/MCSE.2007.55>.
- Islam, Mohammad N., and Deniz Ölçek. 2020. Metrology of Deep Dish Development array (D3A) for precision alignment and surface deformation analysis. In *Ground-based and airborne telescopes viii*, edited by Heather K. Marshall, Jason Spyromilio, and Tomonori Usuda, vol. 11445, 11445J. International Society for Optics and Photonics, SPIE. <https://doi.org/10.1117/12.2562648>. <https://doi.org/10.1117/12.2562648>.
- Larson, K, and Judah Levine. 1998. Time transfer using the phase of the gps carrier [in en]. *IEEE Trans. UFFC*, Pasadena, CA, USA, 1998–01–01 00:01:00. https://tsapps.nist.gov/publication/get_pdf.cfm?pub_id=105365.
- Line, J. L. B., B. McKinley, J. Rasti, M. Bhardwaj, R. B. Wayth, R. L. Webster, D. Ung, et al. 2018. In situ measurement of mwa primary beam variation using orbcomm. *Publications of the Astronomical Society of Australia* 35. issn: 1448–6083. <https://doi.org/10.1017/pasa.2018.30>. <http://dx.doi.org/10.1017/pasa.2018.30>.
- Mackay, Vincent, Mark Lai, Peter Shmerko, Dallas Wulf, Leonid Belostotski, and Keith Vanderlinde. 2023. Low-Cost, Low-Loss, Ultra-Wideband Compact Feed for Interferometric Radio Telescopes. *Journal of Astronomical Instrumentation* 12, no. 4 (January): 2350008. <https://doi.org/10.1142/S2251171723500083>. arXiv: 2210.07477 [astro-ph.IM].
- Marquis, Willard A., and Daniel L. Reigh. 2015. The gps block iir and iir-m broadcast l-band antenna panel: its pattern and performance. *NAVIGATION* 62 (4): 329–347. <https://doi.org/https://doi.org/10.1002/navi.123>. eprint: <https://onlinelibrary.wiley.com/doi/pdf/10.1002/navi.123>. <https://onlinelibrary.wiley.com/doi/abs/10.1002/navi.123>.
- Misra, P., and P. Enge. 2011. *Global positioning system: signals, measurements, and performance*. Ganga-Jamuna Press. isbn: 9780970954428. <https://books.google.com/books?id=5WJOyWAAcAAJ>.
- Raghavan, S.H., M. Shane, and R. Yowell. 2006. Spread spectrum codes for gps l5. In *2006 ieee aerospace conference*, 7 pp.-. <https://doi.org/10.1109/AERO.2006.1655872>.
- Sievers, Jonathan. 2017. *Calibration of quasi-redundant interferometers*. <https://doi.org/10.48550/ARXIV.1701.01860>. <https://arxiv.org/abs/1701.01860>.
- Süzer, Ahmet Esat, and Hakan Oktal. 2017. Prn code correlation in gps receiver. In *2017 8th international conference on recent advances in space technologies (rast)*, 189–193. <https://doi.org/10.1109/RAST.2017.8002960>.
- Tyndall, Will, Alex Reda, J. Richard Shaw, Kevin Bandura, Arnab Chakraborty, Emily Kuhn, Joshua MacEachern, et al. 2024. Beam Maps of the Canadian Hydrogen Intensity Mapping Experiment (CHIME) Measured with a Drone. *arXiv e-prints* (July): arXiv:2407.04848. <https://doi.org/10.48550/arXiv.2407.04848>. arXiv: 2407.04848 [astro-ph.IM].
- United States. Department of Defense. 2020. *Global positioning system standard positioning service performance standard*. Technical report. Accessed: 2024–10–02. United States. Department of Defense, September. <https://www.gps.gov/technical/ps/2020-SPS-performance-standard.pdf>.
- Vanderlinde, Keith, Adrian Liu, Bryan Gaensler, Dick Bond, Gary Hinshaw, Cherry Ng, Cynthia Chiang, et al. 2019. The canadian hydrogen observatory and radio-transient detector (chord) [in en], <https://doi.org/10.5281/ZENODO.3765414>. <https://zenodo.org/record/3765414>.
- Virtanen, Pauli, Ralf Gommers, Travis E. Oliphant, Matt Haberland, Tyler Reddy, David Cournapeau, Evgeni Burovski, et al. 2020. SciPy 1.0: Fundamental Algorithms for Scientific Computing in Python. *Nature Methods* 17:261–272. <https://doi.org/10.1038/s41592-019-0686-2>.
- Wilson, Thomas L., Kristen Rohlf, and Susanne Hüttemeister. 2009. *Tools of Radio Astronomy*. <https://doi.org/10.1007/978-3-540-85122-6>.